Indian Journal of Pure & Applied Physics
Vol. 57, December 2019, pp. 881-890

Estimation of lattice strain in Mn-doped ZnO nanoparticles and its effect on structural and optical properties

Raj Kamal Yadav & Pratima Chauhan*

Department of Physics, University of Allahabad, Allahabad 211 002, India

In this study, Mn-doped ZnO nanoparticles with compositional formula Zn_{1-x} Mn_x O (where, x = 0.00 and 0.10) have been synthesized by simple co-precipitation method. Rietveld refinement of X-ray patterns verifies that the obtained samples have been crystallized in single phase hexagonal wurtzite structure. X-ray peak profile analysis has been used for estimation of crystalline sizes and lattice strain induced by Mn^{2+} doping with the help of Williamson-Hall (W-H) analysis. The morphology of undoped and Mn-doped samples was examined using transmission electron microscopy (TEM) analysis. The mean particle size from TEM results are consistent with results obtained by the Scherrer's formula and W-H analysis. From the optical studies, the absorbance spectra show the increment in energy band gap by Mn^{2+} doping. Photoluminescence (PL) spectra show different emission peaks due to different defect states. This paper heightens the understanding of structural and optical properties of Mn-doped nanoparticles and paves the path for its potential application in modern optoelectronic devices.

Keywords: ZnO, X-ray methods, Rietveld refinement, Electron microscopy, Optical properties

1 Introduction

Zinc oxide (ZnO) is an intrinsic n-type II-VI semiconductor with direct wide band gap 3.37 eV at room temperature (RT). It has large exciton binding energy of 60 meV at RT with good optical properties and stability[1]. Because of its properties, recently it emerged as a novel semiconductor material for ultraviolet (UV) luminescence devices, light emitting diodes (LED), gas sensors, solar cells and transparent thin film transistors[2-6]. ZnO has richest family of its nanostructure. Since, particle size and crystal morphology play great role in their applications, that is why ZnO nanostructures have driven the attention of researchers[7,8]. Several methods have been reported[9] such as sol-gel, precipitation, spray pyrolysis, pyrolysis, DC thermal plasma synthesis, hydrothermal synthesis to prepare ZnO nanopowders. The particle size and morphology will vary with synthesis route adopted for the synthesis of ZnO nanoparticles.

Today, a variety of fruitful approaches like composite and doped semiconductors are developing to modify the physical properties[10-14]. Doping, an intentional incorporation of impurity in host lattice is an effective and most common method to modify the physical properties of host materials for increasing their application in active field of research[15]. There has been a lot of interest in Mn-doped ZnO nanoparticles because of its ferromagnetic behaviour at RT and potential application in spintronics[16]. Recently, a few studies have suggested that Mn-doped ZnO nanoparticles could possess interesting optical properties as well as antibacterial activity[17].

This is because of the change in crystallite size and strain present in the materials which depends on the dopant ions and its concentration, responsible for their valuable behaviour[18]. ZnO nanocrystals morphology, size, level of doping and defect concentrations play crucial role on photoluminescence, photo-catalytic degradation and mechanism of gas sensing for example, high oxygen vacancy concentration is beneficial for photo catalytic, gas sensing and magnetic properties[19-21].

A perfect crystal would extend infinitely in all directions, but no crystals are perfect due to their finite size. This deviation from perfect crystallinity leads to a broadening of the diffraction peaks of materials. There are two main properties extracted from diffraction peak width analysis viz the crystallite size and lattice strain. Crystallite size is a measure of the size of coherently diffracting domain and because of the presence of polycrystalline aggregates the crystallite size of the particles are not generally same as the particle size[22]. The most common techniques used for the measurement of particle size instead of

*Corresponding author (E-mail: mangu167@yahoo.co.in rajkamalyadavo1@gmail.com)

crystallite size are direct light scattering (DLS), scanning electron microscopy (SEM) and transmission electron microscopy (TEM) analysis. Lattice strain is a measure of the distribution of lattice constants arising from crystal imperfections, such as lattice dislocations. There are other sources of lattice strain which are the grain boundary triple junction, stacking faults, contact and sinter stresses, coherency stresses[23], etc. Crystallite size and lattice strain affect the Bragg diffraction peak in different ways and also responsible for increment in the Bragg peak width, intensity and shift the *2θ* peak position accordingly. To estimate the crystallite size and lattice strain, X-ray peak profile analysis (XPPA) is a simple and powerful method[24]. There are some other methods to estimate the crystallite size and lattice strain which are the pseudo-Voigt function, Rietveld refinement and Warren-Averbach analysis[25,26]. Williamson-Hall (W-H) analysis is a simplified integral breadth method[27] used for evaluating crystallite size and lattice strain by considering the peak width as a function of *2θ*. The size-strain plot (SSP) method can also be used to obtain the size-strain parameters. Although, XPPA is an average method, it still holds a dominant position for crystallite size determination apart from TEM analysis.

In this present work, an attempt has been made to understand the effect of Mn^{2+} doping on structural, morphological and optical properties. The strain due to lattice deformation associated with Mn^{2+} doping was studied by Williamson-Hall (W-H) model and size-strain plot (SSP) model. The strain studies of synthesized Mn-doped sample explore the idea of change in optical properties due to strain present in nanocrystals. Photoluminescence (PL) spectra have been carried to observe the role of defects present in synthesized nanoparticles. This study gives the idea of promising application of synthesized Mn-doped ZnO nanoparticles for optoelectronic devices.

2 Experimental Details

2.1 Materials

Zinc acetate dehydrate {$Zn(CH_3COO)_2.2H_2O$ (Rankem, 99.0%)}, manganese acetate tetrahydrate {$Mn(CH_3COO)_2.4H_2O$ (Ranbaxy, 99.0 %)}, sodium hydroxide pallets {NaOH (Merck, ≥ 97 %)} and ethanol (Merck) were used. These precursors were used without further purification. All solutions were prepared using double distilled water (DI water, Merck) as solvent.

2.2 Synthesis of ZnO and Mn-ZnO nanoparticles

Mn-doped ZnO nanoparticles {$Zn_{1-x}Mn_xO$ (where, x = 0.00 and 0.10)} were synthesized by simple co-precipitation method. To prepare undoped ZnO nanoparticles ($Zn_{1-x}Mn_xO$ for x = 0.00), Zn $(CH_3COO)_2.2H_2O$ (548 mg, 0.05 M) was dissolved in 50 ml double distilled water (DI water). In this solution, NaOH (600 mg, 0.3 M) was added dropwise and mixture stirred vigorously for 2 h at 30° C. The resulting solution was allowed to cool and settle down at RT for 24 h. ZnO nanoparticles (white precipitate) were centrifugally collected and washed with DI water and ethanol. Finally, the obtained precipitate was dried at RT. 10 mol% Mn-doped ZnO nanoparticles ($Zn_{1-x}Mn_xO$ for x = 0.10) were prepared using same method. $Zn(CH_3COO)_2.2H_2O$ (548 mg, 0.05 M) and $Mn(CH_3COO)_2.4H_2O$ (61 mg, 0.005 M) were used and followed same procedure as previously described for undoped ZnO nanoparticles.

2.3 Characterization

The X-ray powder diffraction (XRD) analysis of all prepared samples was performed using AXRD bentchtop diffractometer (PROTO manufacturing). The samples were placed on a silicon zero background sample holder and XRD patterns were recorded at RT with CuKα radiation (λ=0.154 nm) over a 2θ range 20°–80°, using angle step size of 0.06°. Fourier transform infrared spectra (FTIR) of all samples were recorded with ABB MB 3000 series FTIR spectrometer (ABB, Bomem, Inc., Québec City, Québec, Canada). For FTIR, the prepared materials were dispersed in DI water and spectra were recorded in the range 4000-400 cm^{-1}. For Transmission electron microscopy (TEM) analysis, synthesized samples were ultrasonically dispersed in DI water to form dilute suspension. TEM images were studied using a Technai G2 20 S-Twin FEI instrument (Czech Republic, operating at 220 kV), by placing a drop of dispersed sample onto carbon coated copper grid. Photoluminescence (PL) spectrum of Mn-doped ZnO nanoparticles was recorded at room temperature using Lab Ram HR Raman Spectrometer (HORIBA Scientific) consisting of He-Cd laser excitation source with power 30 mW at excitation wavelength 325 nm. UV-visible spectroscopy was performed by Ava spec avantes fiber optic spectrometer system.

3 Results and Discussion

3.1 XRD analysis

The crystal structure and phase purity of synthesized undoped and Mn-doped ZnO

nanoparticles (Mn:ZnO) have been analysed by XRD patterns. All the diffraction peaks were indexed to the standard hexagonal wurtzite structure of ZnO (JCPDS No 36-1451, Space group P63mc) shown in Fig. 1. No trace of manganese metal, oxides or any binary zinc manganese phases was found in Mn-doped ZnO samples, which indicates that Mn^{2+} systematically substituted the Zn^{2+} ions without changing the single phase, hexagonal wurtzite structure. There is clear evidence of shifting of peaks towards lower angular scale, which indicates the increase of the lattice parameters. The increment in lattice parameters with Mn doping can be explained by the fact that the ionic radius of doped Mn^{2+} (0.83Å) is larger than that of host ions[28] Zn^{2+} (0.74Å). Moreover, with doping of Mn it was observed that the intensity of diffraction peaks decreased and width broadened also. The decrement of peak intensities and broadening might be due to the decrease of the crystallite size as well as increase in the lattice disorder and strain induced by Mn^{2+} substitution.

The sharp and narrow peak intensity of XRD patterns indicates that prepared samples have small nanocrystals of high quality and good crystallinity. Using XRD data, plane spacing and lattice parameters can be calculated. According to Bragg's law[24]:

$$2d \sin\theta = n\lambda \quad \ldots (1)$$

Where, n is the order of diffraction, λ is the X-ray radiation wavelength and d is interplanar spacing between planes of given miller indices h, k and l. For ZnO hexagonal structure, the interplanar spacing d, lattice parameters a, c and miller indices are related with following equation[24]:

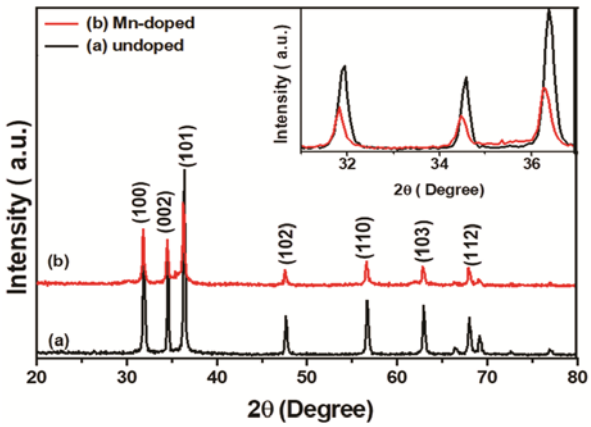

Fig. 1 – X-Ray diffraction patterns of (a) undoped and (b) Mn-doped ZnO nanoparticles.

$$\frac{1}{d^2} = \frac{4}{3}\left(\frac{h^2 + hk + k^2}{a^2}\right) + \frac{l^2}{c^2} \quad \ldots (2)$$

From Eqs (1 and 2), using the first order approximation, $n = 1$,

$$\sin^2\theta = \frac{\lambda^2}{4a^2}\left[\frac{4}{3}\left(h^2 + k^2 + hk\right) + \left(\frac{a}{c}\right)^2 l^2\right] \quad \ldots (3)$$

The lattice constants 'a' and 'c' are calculated for (100) and (002) planes, respectively.

The XRD peak profile analysis is a simple and powerful method to calculate the peak broadening with crystallite size and lattice strain present due to dislocation. The instrumental corrected broadening β_{hkl} corresponding to each diffraction peak of ZnO and Mn-doped ZnO were calculated using the relation[29]:

$$\beta_{hkl} = \left[\left(\beta^2_{hkl}\right)measured - \left(\beta^2_{hkl}\right)instrumental\right]^{1/2} \quad \ldots (4)$$

The average crystallite sizes were calculated from XRD peak width of (101) with the help of Debye-Scherrer equation[30]:

$$D = \frac{k\lambda}{\beta_{hkl}\cos\theta} \quad \ldots (5)$$

Where, β_{hkl} is integral half width, K is a constant called shape factor and equal to 0.91, λ is wavelength of x-ray CuKα source radiation (λ = 0.1540 nm), D is the crystallite size and θ is Bragg angle.

The dislocation density (δ), which denotes the amount of defects in the sample, defines the length of dislocation line per unit volume of the crystals and calculated by using the equation[31]:

$$\delta = \frac{1}{D^2} \quad \ldots (6)$$

The bond length (L) of Zn-O is given by:

$$L = \left[\left(\frac{a^2}{3}\right) + \left(\frac{1}{2} - u\right)^2 c^2\right]^{1/2} \quad \ldots (7)$$

Where, u is the positional parameter in the wurtzite structure and measure the amount of displacement of each atom with respect to next atom along the axis 'c' and given by:

$$u = \frac{a^2}{3c^2} + 0.25 \quad \ldots (8)$$

The reported value of Zn-O bond length[32] in the unit cell of ZnO and its neighbouring atoms is given 1.9767 Å. The calculated bond length for undoped and Mn-doped ZnO samples agrees with reported value as shown in Table 1.

The rietveld refined XRD profiles of undoped ZnO and Mn-doped ZnO nanoparticles are shown in Fig. 2. The rietveld analysis was performed with FULLPROF software and Pseudo-Voigt function is used in order to fit the several parameters to the data points. In order to refine, scale factor, overall B-factor, cell parameters, FWHM parameters, shape parameters etc. were used. The refined patterns are in good agreement with the measured data. No second phase is observed, which revealed that the dopant atoms are incorporated in the wurtzite structure. The low value of χ^2 is showing good fitting of the experimental data. The lattice parameter variation with Mn^{2+} doping was determined from rietveld refinement results and is also listed in Table 2. The change in *c* lattice parameter from 5.2102 Å for pure ZnO to 5.2127 Å for Mn-doped ZnO sample clearly indicates the increase in the lattice size upon doping. Thus, rietveld refinement results are in good agreement with the previous conventional XRD result (Table 1) and relevant interpretations, indicating a possible expansion of ZnO lattice due to substitution of larger Mn^{2+} ions with the Zn^{2+} ions in the lattice.

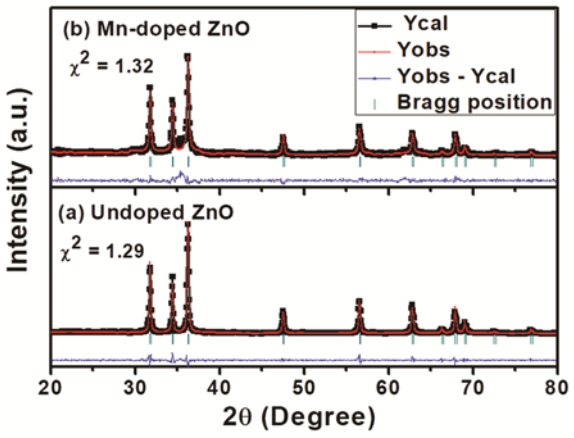

Fig. 2 – Rietveld refinement profiles of XRD data of the (a) undoped and (b) Mn-doped ZnO nanoparticles.

In Table 2, Biso and Occ are isothermal parameter and site occupancy parameter respectively. The fitting quality of the experimental data was evaluated by computing the fitting parameter χ^2. The occupancy values of Zn are listed in Table 2. According to occupancy values, Mn doping leads to a decrease in the Zn occupancy. Therefore, it can be assumed that O vacancies were created due to Mn^{2+} doping. Thus, these occupancy correlations verify the incorporation of Mn^{2+} ions in Zn^{2+} sites. The packing diagram for

Table 2 – Rietveld refined structural parameters for ZnO and 10 mol% Mn^{2+}-doped ZnO nanoparticles

Compound	ZnO	Mn:ZnO
Crystal system	Hexagonal	Hexagonal
Laue class	6/mmm	6/mmm
Point group	6mm	6mm
Bravis lattice	P	P
Lattice symbol	hP	hP
Space group	P63mc (no.186)	P63mc (no.186)
Cell parameters		
a=b (Å)	3.2534	3.2536
c (Å)	5.2102	5.2127
α=β (in degree)	90	90
γ (in degree)	120	120
Direct cell Volume $(Å)^3$	47.760	47.787
Atomic coordinates		
Zn/Mn		
x	0.33333	0.33333
y	0.66667	0.66667
z	0.00000	0.00000
Biso.	3.01231	1.21087
Occ.	1.11351	1.10625
O		
x	0.33333	0.33333
y	0.66667	0.66667
z	0.38485	0.39844
Biso.	0.58199	0.49728
Occ.	0.99983	1.00045
χ^2	1.29	1.32
Density of compound (g/cc)	5.542	5.553

Table 1 – The effect of Mn-doping on unit cell parameters, crystallite size, dislocation density and bond length.

Mn doping (%)	Unit cell parameters		Cell volume ($Å^3$)	c/a ratio	Crystallite size *D* (nm)	Dislocation density (δ) 10^{-4} (nm^{-2})	Bond length *L* (Å)
	a (Å)	c (Å)					
0	3.2367	5.1864	47.0531	1.6023	37.76	7.0135	1.9699
10	3.2447	5.1969	47.3817	1.6016	31.91	9.8203	1.9745

undoped ZnO nanoparticles was drawn using VESTA (Visualization for Electronic and Structural Analysis) software as shown in Fig. 3 (a and b).

3.2 Estimation of microstrian (ε)

3.2.1 Williamson-hall (W-H) methods

Uniform deformation model (UDM)

In addition to the instrumental X-ray peak broadening, crystallite size and lattice strain are extra two factors which contribute in total diffraction line broadening. According to Williamson and Hall methodology, the diffraction line broadening is due to the crystallite size and strain present in the material. The strain induced line broadening β_ε due to crystal imperfection and distortion[27] is given by:

$$\beta_\varepsilon = 4\varepsilon \tan\theta \quad \ldots (9)$$

From scherrer Eq. (5), it was confirmed that the broadening due to crystallite size β_D varies with $1/cos\theta$ and from above Eq. (9), it is shown the strain induced broadening β_ε it varies with $tan\theta$.

Assuming the uniformity of strain in material, (i.e., isotropic nature of the crystal), the Williamson-hall equation[33] for the total peak broadening is given by

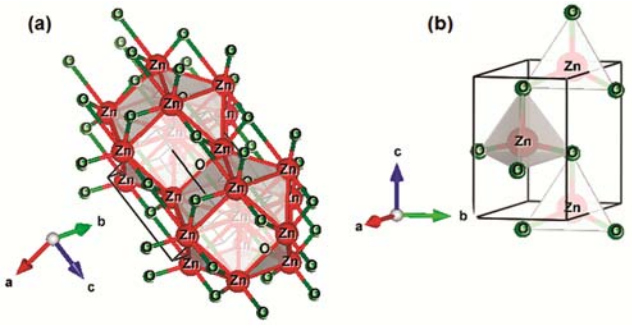

Fig. 3 – (a) Schematic diagram of undoped ZnO complex structure drawn by VESTA software and (b) unit cell of undoped ZnO.

$$\beta_{hkl} = \beta_D + \beta_\varepsilon \quad \ldots (10)$$

Where, β_{hkl} is peak width at half maximum intensity of instrumental corrected broadening. If we assume that the particle size and strain contributions to line broadening are independent to each other and both have a cauchy-like profile, the observed line width is simple addition[34] of Eq. (5 and 9) and written as:

$$\beta_{hkl} = \frac{k\lambda}{D\cos\theta} + 4\varepsilon \tan\theta \quad \ldots (11)$$

Rearranging Eq. (11) gives:

$$\beta_{hkl}\cos\theta = \frac{k\lambda}{D} + 4\varepsilon \tan\theta \quad \ldots (12)$$

Equation (12) is known as Williamson-hall equation, which represents the uniform deformation model (UDM). UDM is an appropriate model for calculating microstrain present in the crystal assuming strain which is uniform in all direction of the crystal system. This model considers that the crystal is isotropic in nature and material properties do not change with direction along which it is measured. The graphs were plotted between $\beta_{hkl}\,Cos\theta$ and $4\,Sin\theta$ for preferred diffraction peaks for undoped and Mn-doped ZnO nanoparticles. In W-H-UDM model, the strain ε present in the material and the crystallite size D are, respectively calculated from slope and y- intercept of linear fit data plot. The UDM for undoped and Mn-doped ZnO nanoparticles are shown in Fig. 4 (a and b), respectively.

Uniform stress deformation model (USDM)

In USDM model, the lattice deformation stress is supposed to be uniform in all crystallographic directions. For more realistic condition, consider microstrian to be anisotropic. Therefore, Williamson

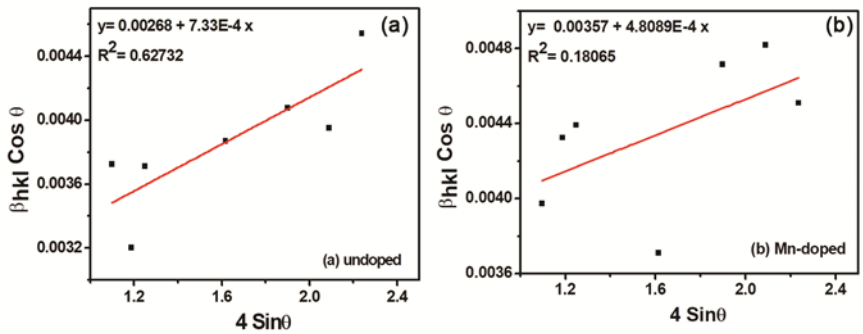

Fig. 4 – Plot of $\beta_{hkl}\,cos\theta$ versus $4\,sin\theta$ for (a) undoped and (b) Mn-doped ZnO nanoparticles.

hall equation is modified by an anisotropic strain[35]. It is assumed that a small microstrain is present in synthesized ZnO and Mn doped ZnO nanoparticles. In this model, the Hook's law maintaining the linear proportionality between stress and strain as given by $\sigma = \varepsilon Y_{hkl}$, where σ is the stress of the crystal, ε is anisotropic microstrain and Y_{hkl} is the modulus of elasticity. By Hook's approximation, the Williamson-Hall equation is modified[34], and we get:

$$\beta_{hkl} \cos \theta_{hkl} = \frac{K\lambda}{D} + \frac{4\sigma \sin \theta_{hkl}}{Y_{hkl}} \quad \ldots (13)$$

Plotting the ($\beta_{hkl} \cos \theta_{hkl}$) as a function of ($4\sin\theta_{hkl} / Y_{hkl}$) shown in Fig. 5, the uniform deformation stress σ can be calculated from the slope of the linear fit and y-intercept gives the crystallite size. The strain ε can be measured if modulus of elasticity Y_{hkl} is known for hexagonal ZnO and Mn:ZnO nanoparticles. Samples having hexagonal phase, modulus of elasticity Y_{hkl} is related to their elastic components[23,26] S_{ij} as:

$$Y_{hkl} = \frac{\left[h^2 + (h+2k)^2 + \left(\frac{al}{c}\right)^2\right]^2}{s_{11}\left(h^2 + \frac{(h+2k)^2}{a}\right)^2 + s_{33}\left(\frac{al}{c}\right)^4 + (2s_{13} + s_{44})\left(h^2 + \frac{(h+2k)^2}{3}\right)\left(\frac{al}{c}\right)^2} \quad \ldots (14)$$

Where, s_{11}, s_{13}, s_{33} *and* s_{44} are the elastic compliances[36] of ZnO having values 7.858×10^{-12}, 2.206×10^{-12}, 6.940×10^{-12} and 23.57×10^{-12} m^2N^{-1}, respectively.

Uniform deformation energy density model (UDEDM)

The uniform deformation energy density model (UDEDM) can be used to conclude the energy density of a crystal. In Eq. (12), we assumed the homogeneous isotropic nature of crystal; however, in many cases, this assumption is not justified. Moreover, the constant of proportionality associated with the stress-strain relation are no longer independent when the strain energy density u_{ed} is considered. For the system obeys Hook's law, the energy density u_{ed} as a function of strain is given by $u_{ed} = \varepsilon^2 Y_{hkl}/2$. Therefore, Eq. (13) can be modified in Eq. (15) as given below:

$$\beta_{hkl} \cos \theta_{hkl} = \frac{K\lambda}{D} + \left(4 \sin \theta_{hkl} \left(2u_{ed} / Y_{hkl}\right)^{1/2}\right) \quad \ldots (15)$$

The anisotropic energy density u_{ed}, crystallite size D were estimated by plotting graph between $\beta_{hkl} \cos\theta_{hkl}$ and 4 $\sin\theta_{hkl}$ $(2/Y_{hkl})^{1/2}$, shown in Fig. 6. The lattice strain can be calculated by knowing the modulus of elasticity Y_{hkl} of the samples.

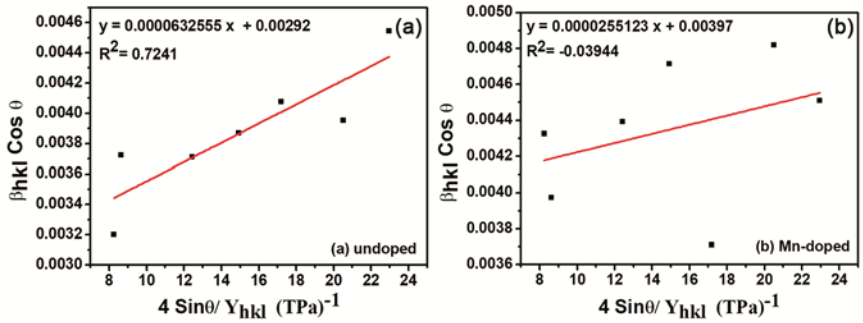

Fig. 5 – Plot of $\beta_{hkl} \cos\theta_{hkl}$ versus $4 \sin\theta_{hkl} / Y_{hkl}$ for (a) undoped and (b) Mn-doped ZnO nanoparticles.

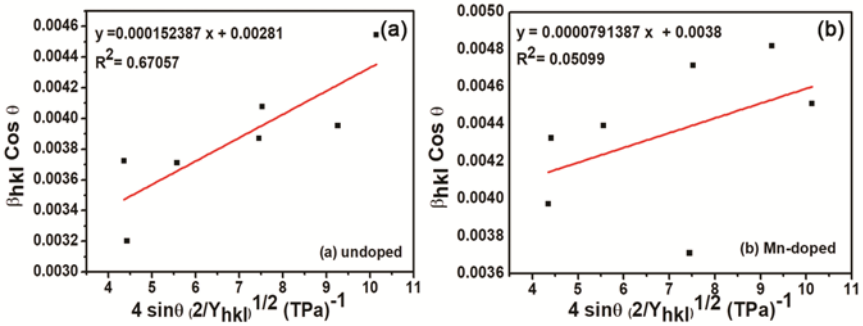

Fig. 6 – Plot of $\beta_{hkl} \cos\theta_{hkl}$ versus 4 $\sin\theta_{hkl}$ $(2/Y_{hkl})^{1/2}$ for (a) undoped and (b) Mn-doped ZnO nanoparticles.

Size-strain plot (SSP) method

The W-H Plots represented that the line broadening was basically isotropic. This accentuates that the diffracting domain were isotopic because of microstrain contribution. The size-stain plot was used to obtain size-strain parameters for isotropic line broadening. This method has an advantage that less importance is given to data from reflection at high angles because of lower precision. In SSP method, it is assumed that the 'strain profile' is described by a Gaussian function and the 'crystallite-size' by a Lorentzian function[37]. Hence, we have:

$$\left(d_{hkl}\beta_{hkl}\cos\theta_{hkl}\right)^2 = \frac{1}{V_s}\left(d_{hkl}^2\beta_{hkl}\cos\theta_{hkl}\right)+\left(\frac{\varepsilon_a}{2}\right)^2 \quad \ldots (16)$$

Where, d_{hkl} is interplanar spacing for *(h k l)* planes, V_s is the apparent volume weighted average size related with D_v for spherical crystallites as $D_v = V_s(4/3)$ and ε_a is a measure of apparent strain which is related with root-mean-square (RMS) strain ε_{RMS} by $\langle\varepsilon_{RMS}\rangle = \left(\varepsilon_a / 2(2\pi)^{1/2}\right)$.

In Fig. 7, The SSP were obtained for ZnO and Mn:ZnO nanoparticles respectively, by plotting graph between $(d_{hkl}\,\beta_{hkl}\,cos\,\theta_{hkl})^2$ on y-axis and $(d^2_{hkl}\beta_{hkl}\,cos\,\theta_{hkl})$ on x-axis for all peaks of ZnO and Mn:ZnO nanoparticles with wurtzite hexagonal phase from 2θ to 20°–80°. The volume averaged crystallite size is estimated from the slope of linearly fitted data and the strain from y-intercept.

3.3 Transmission electron microscopy (TEM) method

The morphological study of as-obtained ZnO and Mn doped ZnO nanoparticles were analysed by TEM. The TEM micrograph of ZnO and Mn-doped ZnO nanoparticles are shown in Fig. 8. It is observed in Fig. 8(a), the ZnO sample is mainly composed of spherical/ellipsoidal and few hexagonal shapes like morphology with an average particle size 40 nm. Decease in nanoparticles size to 23 nm was observed in Fig. 8(b) for Mn-doped ZnO nanoparticles (10 mol %). This decrease in particle size may be ascribed to the limited growth of the nanocrystals due to the presence of dopant ions in the reaction medium[38,39]. Histogram diagram (shown in Fig. 9) of undoped and Mn-doped ZnO nanoparticles is drawn with the help of TEM image. The results obtained from Williamson-hall method, size-strain plot method and TEM are summarized in Table 3.

3.4 FTIR analysis

The composition, quality and molecular structure of the synthesized materials were analysed by ABB Bomem FTIR MB 3000 spectrometer. The FTIR measurements of both samples were performed in the wave number range from 400 to 4000 cm^{-1}. The wide-

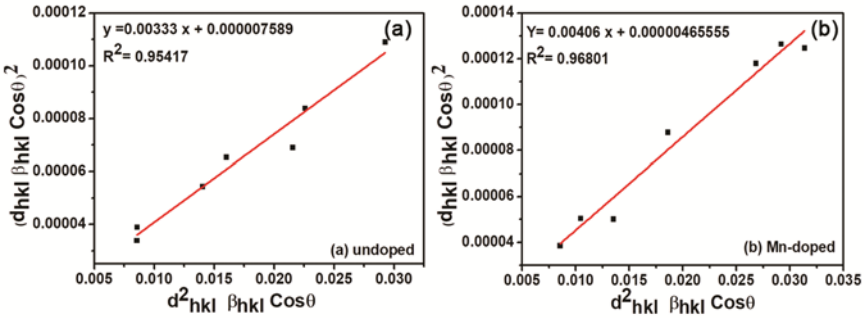

Fig. 7 – Plot of $(d_{hkl}\,\beta_{hkl}\,cos\,\theta_{hkl})^2$ versus $(d^2_{hkl}\beta_{hkl}\,cos\,\theta_{hkl})$ for (a) undoped and (b)Mn-doped ZnO nanoparticles.

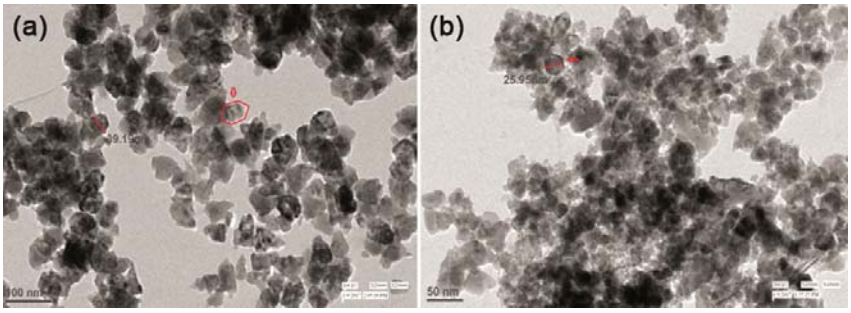

Fig. 8 – TEM micrograph of (a) undoped and (b) Mn-doped ZnO nanoparticles.

ranging absorption peak around 3395 cm^{-1} represents the stretching mode of the O-H group of H_2O, indicating the water absorbance on surface of nanocrystalline powder. The absorption peak around 1649 cm^{-1} is attributed to H-O-H bending vibration, which is assigned to a small amount of water in ZnO nanocrystals[40]. In Fig. 10, we observed very strong bands at 464 cm^{-1} and 457 cm^{-1} , are assigned for the stretching modes of Zn-O and (Zn, Mn)-O, respectively[41,42]. Here, in this study we observed small shift in band position due to the substitution of Mn^{2+} ion into the Zn-O lattice.

3.5 UV-visible spectroscopy

Absorption spectroscopy is an influential method to study the optical properties of nanoparticles. Figure 11 shows the Uv-Vis absorption spectra of (a) undoped and (b) Mn-doped ZnO nanoparticles with absorption edges 367 and 356 nm, respectively. The absorption edge of doped sample is blue shifted as compare to undoped ZnO sample. The blue shift in the absorption band edge is generally explained by the quantum confinement properties of nanomaterials. In quantum confinement range, the band gap of the particles increases as the particle size decreases[43]. The optical band gap for Mn-doped ZnO nanoparticles was determined by using the formula[44]:

$$(\alpha h\nu)^2 = A(h\nu - E_g) \quad \ldots (17)$$

Where, α is absorption coefficient, A is constant and E_g is the optical band. From Eq. (17), Tauc plot can

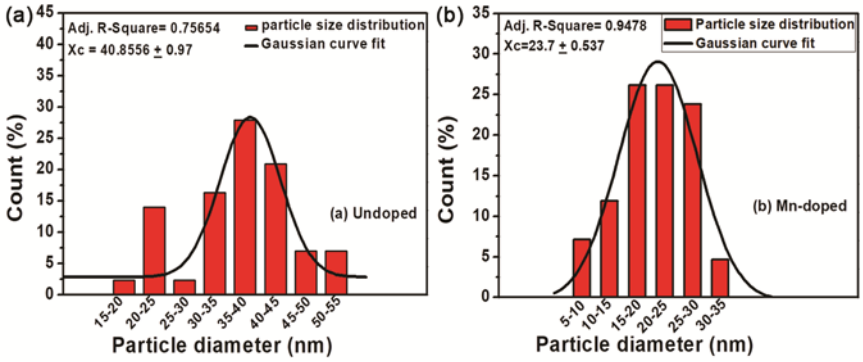

Fig. 9 – Histogram diagram of (a) undoped and (b) Mn-doped ZnO nanoparticles.

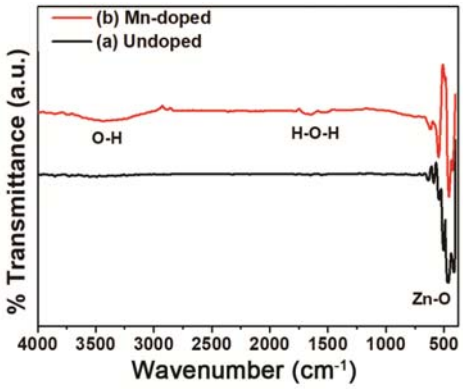

Fig. 10 – FTIR spectrum of (a) undoped and (b) Mn-doped ZnO nanoparticles.

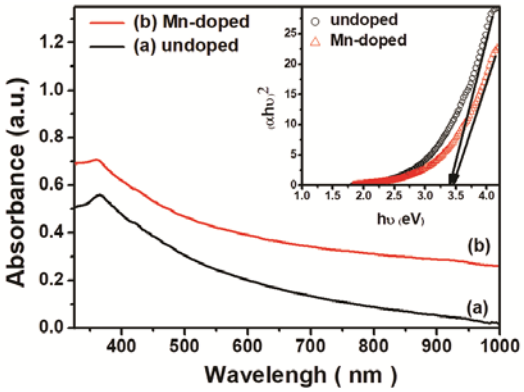

Fig. 11 – UV-visible absorption spectra of (a) undoped and (b) Mn-doped ZnO nanoparticles.

Table 3 – Geometric parameters of synthesized undoped and Mn-doped ZnO nanoparticles

Sample name Mn (%)	Scherrer method D (nm)	Williamson-hall method									Size-strain plot			TEM D (nm)
		UDM		USDM			UDEDM				D_v (nm)	ε		
		D (nm)	ε x10^{-4}	D (nm)	ε x10^{-4}	σ (MPa)	D (nm)	ε x10^{-4}	σ (MPa)	u (kJm^{-3})		ε_a x10^{-3}	ε_{RMS} x10^{-4}	
0	37.76	52.2	7.33	48.0	4.97	63.25	49.8	6.04	76.87	23.22	40.0	5.51	10.6	40
10	31.91	39.2	4.81	35.3	2.00	25.51	35.3	3.13	39.92	6.26	32.8	4.31	8.6	23

be drawn of $(\alpha h\upsilon)^2$ versus $h\upsilon$ as shown in inset of Fig. 11. The optical band gap may be obtained from extrapolation of linear portion of tauc plot. The obtained optical band gaps are 3.39 eV and 3.48 eV for undoped and Mn-doped ZnO nanoparticles, respectively. Hence, obtained result indicates that the bandgap of ZnO increases by doping of Mn^{+2} ions.

3.6 Photoluminescence (PL) spectroscopy

The optical emission properties of the Zn_{1-x} Mn_xO (x=0 and 10 mol %) were investigated by PL spectroscopy (Fig. 12) using a 325 nm excitation wavelength of He-Cd laser at room temperature (RT). There appeared an intense narrow emission band in UV spectral range at 381 nm and 379 nm for ZnO and Mn:ZnO samples, respectively. Generally, the near band emission in UV region originates due to the recombination of free excitons in ZnO and Mn:ZnO samples[45]. A very small blue shift in UV band has been observed, which is consistent with the analysis of UV-visible absorption spectra. Apart from sharp UV emission band, there appeared another wider emission band in the visible spectral range near 543 nm and 533 nm. This visible emissions of ZnO and Mn:ZnO nanoparticles originated from the recombination of electron-hole associated with the intrinsic defects in ZnO such as oxygen vacancy (V_O), oxygen interstitial (O_i), zinc vacancy (V_{Zn}), zinc interstitial (Zn_i) and antisite oxygen (O_{Zn}) in nanoparticles[46]. Another band appeared near 764 nm and 770 nm for ZnO and Mn:ZnO samples, respectively. The origin of these bands are very controversial because some authors[47] have attributed it to V_O while some other authors attributed it to oxygen and zinc anti-sites[48,49]. Some other authors have proposed that such emission is a second-order feature of the UV emission[50,51]. It is observed that PL

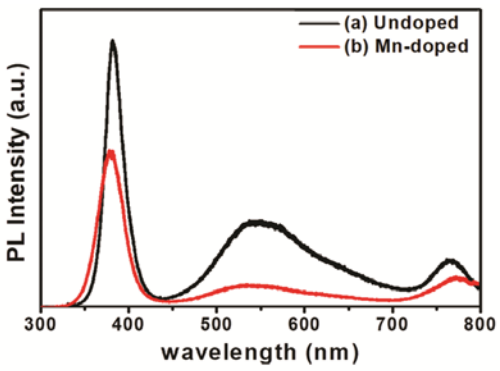

Fig. 12 – Photoluminescence (PL) spectra of (a) undoped and (b) Mn-doped ZnO nanoparticles.

intensity have been reduced by Mn-doping. This indicates the increment in defect concentration and poor crystallization caused by Mn-doping[52]. Since, photoluminescence is closely related with the recombination of the photo-generated electron-hole pairs. The weaker PL intensity of Mn doped sample indicates the slower recombination of electron-hole pairs. This is because that the Mn^{2+} ions provide several electron traps to suppress the recombination of photo-generated electron-hole pairs. The Mn^{2+} doped ZnO nanoparticles have a lower recombination rate and improved optical properties in compare to pure ZnO nanoparticles. Therefore Mn^{2+} doped ZnO nanoparticles can be a good candidate for efficient solar cells fabrication[53].

4 Conclusions

ZnO and Mn-doped ZnO nanoparticles have been prepared by co-precipitation method and characterized by XRD, TEM, FTIR, UV-Vis absorption and photoluminescence spectroscopy. The X-ray diffraction patterns revealed that the nanoparticles for both samples are crystallized in hexagonal wurtzite ZnO structure, which is also confirmed by rietveld analysis. The lattice parameters 'a' and 'c' increase with Mn doping which indicates that Mn^{2+} ions substitutes Zn^{2+} ions. The occupancy correlations given by rietveld analysis in Table 2 also confirms the incorporation of Mn^{2+} ions in Zn^{2+} sites. The line broadening of undoped and Mn-doped ZnO nanoparticles were due to small crystallite size and strain. This broadening was analysed by the scherrer method, W-H methods and SSP method. From the results discussed in Table 3, it was observed that strain as well as crystallite size value decreased with Mn doping. The lattice strain ε calculated from W-H and SSP methods was found to be nearly alike and in agreement with each other. In W-H analysis, the average value of crystallite size obtained from UDM, USDM and UDEDM are nearly comparable. The W-H model was also used to estimate lattice deformation stress and lattice deformation energy density of samples. The TEM images of ZnO and Mn-doped ZnO nanoparticles reveal the average particle size to be 40 nm and 23 nm, respectively and these results are in good agreement with the results of the W-H and SSP methods. In all models, SSP model have shown best agreement with the TEM result. The IR peaks were analysed and assigned. The small shift observed in FTIR bands by Mn-doping may be due to the Zn-O-Mn stretching. A significant change in optical properties of ZnO nanoparticles have been

observed by Mn doping. UV-Vis measurement revealed that the band gap increased due to incorporation of Mn^{2+}. PL spectra of Mn-doped ZnO exhibited small blue shift in peaks in compare to the undoped ZnO nanoparticles. In short, this paper gives an easy and fast way to synthesize Mn-doped ZnO nanoparticles. Optical and structural properties of spherical/ hexagonal shaped Mn-doped ZnO nanoparticles display high interest for new technological applications.

Acknowledgement

The authors are thankful to University Grant Commission (UGC), New Delhi for financial support to carrying out this research work. The authors gratefully acknowledge the Head, Department of Physics for providing departmental facilities. We are also acknowledging AIIMS (SAIF), New Delhi for providing TEM facility.

References

1 Xu F, Lu Y, Xie Y & Liu Y, *Vacuum*, 83 (2009) 360.
2 El Ghoul J, Barthou C & El M L, *Physica E*, 44 (2012) 1910.
3 Khorsand Z A, Abd M W H, Abrishami M E, Yousefi R & Parvizi R, *Solid State Sci*, 14 (2012) 488.
4 Li J, Fan H, Chen X & Cao Z, *Colloids Surf A*, 349 (2009) 202.
5 Sharma S & Chauhan P, *AIP Conf Proc*, 1724 (2016) 020106.
6 Arora A & Deshwal M, *Indian J Pure Appl Phys*, 57 (2019) 422.
7 Hotchandani S & Kamat P V, *J Phys Chem ,* 96 (1992) 6834.
8 Sakohapa S, Tickazen L D & Anderson M A, *J Phys Chem*, 96 (1992) 11086.
9 Niasari M S, Davar F & Mazaheri M, *Mater Lett*, 62 (2008) 1890.
10 Achouri F, Corbel S, Aboulaich A, Balan L, Ghrabi, Ben S M & Schneider R, *J Phys Chem Solids* 75 (2014) 1081.
11 Jeena V & Robinson R S, *Chem Commun,* 48 (2012) 299.
12 Wang F, Liang L, Shi L, Liu M & Sun J, *Dalton Trans,* 43 (2014) 1644.
13 Anandan S & Miyauchi M, *Phys Chem Chem Phys,* 13 (2011) 14937.
14 Bloh J Z, Dillert R & Bahnemann D W, *Environ Sci Pollut Res,* 19 (2012) 3688.
15 Chen J T, Wang J, Zhuo R F, Yan D, Feng J J, Zhang F & Yan P X, *Appl Surf Sci,* 255 (2009) 3959.
16 Dietl T, Ohno H, Matsukura F, Cibert J & Ferrand E D, *Science*, 287 (2000) 1019.
17 Rekha K, Nirmala M, Nair M G & Anukaliani A, *Physica B: Condensed Matter*, 405 (2010) 3180.
18 Hao Y M, Lou S Y, Zhou S M , Yuan R J, Zhu G Y & Li N, *Nano Res Lett,* 7 (2012) 1.
19 Lai Y, Meng M, Yu Y, Wang X & Ding T, *Appl Catal B: Environ*, 105 (2011) 335.
20 Iqbal J, Wang B, Liu X, Yu D, He B & Yu R H, *New J Phys,* 11 (2009) 063009.
21 Chang C M, Hon M H & Leu I C, *Sens Actuators B: Chem,* 151 (2010) 15.
22 Hebbar K R, *Basics of X-ray diffraction and its applications*, (I K International Publishing House Pvt Ltd: New Dehli) 1st Edn, (2007) 254.
23 Warren B E & Averbach B L, *J Appl Phys,* 21 (1950) 595.
24 Cullity B D & Stock S R, *Elements of X-ray diffraction*, (Pearson Education Limited: USA) 3rd Edn, (2001) 97.
25 Rietveld H M, *Acta Crystallogr,* 22 (1967) 151.
26 Balzar D & Ledbetter H J, *J Appl Cryst,* 26 (1993) 97.
27 Suryanarayana C & Norton M G, *X-ray diffraction: A practical approach*, (Springer: US, New York), 1st Edn, (1998) 240.
28 Luo J, Liang J K, Liu Q L, Liu F S, Zhang Y, Sun B J & Rao G H, *J Appl Phys,* 97 (2005) 086106.
29 Rogers K D & Daniels P, *Biomaterial,* 23 (2002) 2577.
30 Saleem M, Fang L, Ruan H B, Wu F, Huang Q L, Xu C L & Kong C Y, *Intl J Phys Sci*, 7 (2012) 2971.
31 Barret C S & Massalski T B, Structure of metals: *Crystallographic methods, principles and data*, (Pergamon Press: Oxford), 3rd Edn, (1980) 427.
32 Seetawan U, Jugsujinda S, Seetawan T, Ratchasin A, Euvananont C, Junin C, Thanachayanont C & Chainaronk P, *Mater Sci Appl, 2* (2011) 1302.
33 Hingorani S, Pillai V, Kumar P, Multani M S & Shah D O, *Mater Res Bull,* 12 (1993) 1303.
34 Pandiyarajan T & Karthikeyan B, *J Nanopart Res,* 1 (2012) 647.
35 Bindu P & Thomas S, *J Theor Appl Phys*, 4 (2014) 123.
36 Nye J F, Physical properties of crystals: *Their representation by tensors and matrices*, (Oxford University Press: USA), 1st Edn, (1985)147.
37 Tagliente M A & Massaro M, *Nucl Instrum Methods Phys Res B,* 7 (2008) 1055.
38 Dar M I, Arora N, Singh N P, Sampath S & Shivashankar S A, *New J Chem*, 10 (2014) 4783.
39 Moussa H, Merlin C, Dezanet C, Balan L, Medjahdi G, Ben-Attia M & Schneider R, *J Hazard Mater*, 304 (2016) 532.
40 Raja K, Ramesh P S & Geetha D, *Spectrochim Acta A: Mol Biomol Spectrosc*, 131 (2014) 183.
41 Maensiri S, Laokul P & Promarak V, *J Cry Growth,* 289 (2006) 102.
42 Suwanboon S, *Science Asia*, 34 (2008) 31.
43 Singla M L & Kumar M, *J Lumin*, 129 (2009) 434.
44 El G J, Barthou C & El M L, *Physica E*, 44 (2012) 1910.
45 Ton-That C, Foley M & Phillips M R, *Nanotechnology,* 19 (2008) 415606.
46 Dietrich C P, Brandt M, Lange M, Kupper J, Böntgen T, von Wenckstern H & Grundmann M, *J Appl Phys*, 109 (2011) 013712.
47 Wu B, Li J & Li Q, *Optik,* 188 (2019) 205.
48 Singh J, Rathi A, Rawat M, Kumar V & Kim K H, *Compos Part B: Eng*, 166 (2019) 361.
49 Kumar V, Swart H C, Ntwaeaborwa O M, Kroon R E, Terblans J J, Shaat S K, Yousif A & Duvenhage M M, *Mater Lett*, 101 (2013) 57.
50 Cross R B, De Souza M M & Narayanan E S, *Nanotechnology*, 16 (2005) 2188.
51 Mahalingam T, Lee K M, Park K H, Lee S, Ahn Y, Park J Y & Koh K H, *Nanotechnology,*18 (2007) 035606.
52 Lang J, Han Q, Li C, Yang J, Li X, Yang L, Wang D, Zhai H, Gao M, Zhang Y & Liu X, *Appl Surf Sci*, 256 (2010) 3365.
53 Fabbiyola S & Kennedy L J, *J Nanosci and Nanotechnol,* 19 (2019) 2963.